Shear-induced breaking of cages in colloidal glasses: Scattering experiments and mode coupling theory

Christian P. Amann,[1,a)] Dmitry Denisov,[2] Minh Triet Dang,[2] Bernd Struth,[3] Peter Schall,[2] and Matthias Fuchs[1,b)]
[1]*Fachbereich Physik, Universität Konstanz, 78457 Konstanz, Germany*
[2]*Van der Waals-Zeeman Institute, University of Amsterdam, Amsterdam, The Netherlands*
[3]*Deutsches Elektronen-Synchrotron, Hamburg, Germany*

(Received 9 February 2015; accepted 6 July 2015; published online 21 July 2015)

We employ x-ray scattering on sheared colloidal suspensions and mode coupling theory to study structure factor distortions of glass-forming systems under shear. We find a transition from quadrupolar elastic distortion at small strains to quadrupolar and hexadecupolar modes in the stationary state. The latter are interpreted as signatures of plastic rearrangements in homogeneous, thermalized systems. From their transient evolution with strain, we identify characteristic strain and length-scale values where these plastic rearrangements dominate. This characteristic strain coincides with the maximum of the shear stress versus strain curve, indicating the proliferation of plastic flow. The hexadecupolar modes dominate at the wavevector of the principal peak of the equilibrium structure factor that is related to the cage-effect in mode coupling theory. We hence identify *the* structural signature of plastic flow of glasses. © *2015 AIP Publishing LLC.* [http://dx.doi.org/10.1063/1.4926932]

I. INTRODUCTION

The equilibrium structure of quiescent colloidal dispersions is determined by particle interactions and packing constraints; yet, externally imposed flows can easily distort the local structure if the applied flow rates compete with structural relaxation rates. These flow-induced distortions provide important information on the mechanisms of structural rearrangements and on the average particle motion underlying them. While strong flows cause various ordering phenomena,[1] weak flows leave even concentrated systems homogeneous and amorphous.[2] The stationary structure then reveals in which way quiescent (rigid) units are broken up by the flow-induced motion. It encodes average effects of the plastic deformation, signatures that are difficult to identify in glass-forming systems.

Dense colloidal suspensions serve as good models for glasses[3] due to their large length and long time scales. Confocal microscopy has proven especially valuable to observe inhomogeneous structural correlations[4–10] and to follow the single particle dynamics,[2,11,12] with computer simulations providing support and additional information.[13–16] To study average structural effects, especially when structural changes are small, scattering experiments are the better choice since they typically average over larger sample volumes and achieve more accurate structure factors via natural interference. For soft glasses such as colloidal suspensions, small angle x-ray scattering can detect intermediate-range periodicities of the particle packings and thus addresses the relevant length scales involved in the structural processes. While for states deep in the glass, a consistent description of plastic flow starts to emerge for individual plastic events and their coupling when their density is low (possibly explaining shear-localization), less is known about states closer to the glass transition, where thermal fluctuations are important, and where a description of the ensemble of plastic events is required. In particular, structural signatures of the emerging flow are difficult to identify in amorphous materials, and remain elusive, even in colloidal glasses.

Here, we report a joint investigation of x-ray diffraction experiment and mode coupling theory (MCT) identifying the shear-induced structural changes in colloidal glass-forming dispersions. We focus on states close to the colloidal glass transition and apply small shear rates $\dot{\gamma}$, which nevertheless exceed the inverse structural relaxation time τ and hence induce significant structural distortions. We observe significant distortion of the nearest-neighbor structure that encodes structural signatures of the highly nonlinear macroscopic stress response, which we measure simultaneously by recording steady-state flow curves. By following this distortion as a function of applied strain starting from the quiescent state, we identify a characteristic symmetry change from the initial elastic state to the shear-melted steady state. While the initial elastic response exhibits the generically expected quadrupolar angular symmetry, the plastically deforming state shows a strong nonlinear hexadecupolar contribution with the periodicity of the packing. This symmetry change heralds the onset of plastic deformation and is the strongest just before the stress-release which leads to the well-known maximum of the macroscopic stress-strain curve (often termed stress-overshoot). We interpret the hexadecupolar signal as a good indicator of plastic events and suggest a microscopic picture of particle motion underlying the ensemble-averaged plastic deformation.

a)Christian.2.Amann@uni-konstanz.de
b)Matthias.Fuchs@uni-konstanz.de

II. METHODS

A. Mode coupling theory of the shear distorted structure

Under already weak flows, the average structure of highly concentrated colloidal dispersions is distorted. This occurs because the flow rate $\dot\gamma$ may far exceed the inverse of the structural relaxation time τ. Their ratio is measured by the Weissenberg or dressed Peclet number $\mathrm{Pe} = \dot\gamma\tau$. At $\mathrm{Pe} > 1$, flow-induced particle transport starts to dominate the thermal relaxation, and the resulting stationary structure becomes anisotropic and differs from the quiescent isotropic one. Yet, the structure remains amorphous and homogeneous if ordering phenomena are suppressed by, e.g., polydispersity, and as long as shear rates are small compared to the inverse of the single-particle diffusion time. The ratio of both is given by the bare Peclet number $\mathrm{Pe}_0 = \dot\gamma t_B$,[2,14] built with the Brownian diffusion time t_B of the initial small-distance diffusion of individual colloids.

MCT as developed by Götze and coworkers provides a microscopic description of the quiescent structural relaxation using canonically ensemble-averaged correlation functions.[17] This approach appears best suited to homogeneously rearranging amorphous structures. It predicts an ideal glass transition caused by a feedback-mechanism corresponding to cooperative caging of particles in neighbor shells. The mechanism is often termed "cage-effect." Its relevant length scales are (i) the average particle separation which enters the scale on which the structural rearrangements are coupled most strongly and (ii) the localization length, which describes the range of cooperative rearrangements possible in the solid state. While the first is well known from measures of the equilibrium structure of fluids (like the equilibrium structure factor, where its inverse gives the position of the principal peak), the latter is a dynamical length scale only visible in time-dependent measurements. Reminiscent of Lindemann's criterion of melting of simple crystals, MCT finds that the ratio of both length scales at the glass transition is around 10%. Dynamic light scattering studies have shown that around 58% volume fraction colloidal hard spheres exhibit many of the theoretical predictions, and that MCT's "cage-effect" scenario correlates many observations.[18–20]

The application of external deformations like shear combined with investigation of the particle-scale structure now provides a unique tool to test the "cage-effect" picture beyond its original regime where it was developed. To account for the macroscopically observed shear-induced melting of colloidal glasses, the cages need to be opened by shear. This leads to shear-induced diffusive motion (in all three spatial directions) and to ergodic structural relaxation. This deformation mode will be called plastic in the following. The difference between structural correlations in stationary flow and in the quiescent equilibrium state thus detects the yielding of cages and the ensemble-averaged plastic events.

Assuming homogeneous flow deformations, MCT has been generalized to shear-driven systems in the integration-through-transients (ITT) formalism. It calculates the complete time evolution of a concentrated dispersion under arbitrary time-dependent strain deformation; the approach and its comparisons with rheological experiments have been reviewed in Refs. 21 and 22. The MCT-ITT approach by Ref. 23 neglects hydrodynamic interactions reasoning that at high particle densities, structural correlations dominate over hydrodynamic ones. Solvent effects are argued to renormalize the hydrodynamic radii and short time diffusion coefficients. The transient density correlator $\Phi_{\mathbf{q}}(t) = \langle \rho^*_{\mathbf{q}} \rho_{\mathbf{q}(t)}(t)\rangle / N S_q$ is the central object of the theory and provides a description of the motion of the particles. It is a correlation function built with density fluctuations, $\rho_{\mathbf{q}} = \sum_{j=1}^{N} \exp\{i\mathbf{q}\cdot\mathbf{r}_j\}$, averaged with the canonical equilibrium distribution. The normalization to $\Phi_{\mathbf{q}}(0) = 1$ is given by the equilibrium structure factor S_q. The equation of motion of $\Phi_{\mathbf{q}}(t)$ contains rapid local motion without structural decay and elasticity and plasticity during structural rearrangements. The shear-advected wavevector $\mathbf{q}(t) = (q_x, q_y - \dot\gamma t q_x, q_z)^T$ appearing in the definition accounts for the affine particle motion with the flow. It is a central prediction of MCT-ITT that this time-dependence shifts density modes to higher and higher wavevectors with time, where their coupling is weaker. Thereby, the feedback-mechanism in MCT's cage-effect is cut off and structural relaxation becomes possible (in non-ergodic states) or accelerated (in general). In MCT-ITT, the competition between particle caging and shear advection of fluctuations is given by a non-Markovian equation of motion containing a retarded friction kernel,

$$\dot\Phi_{\mathbf{q}}(t) + \Gamma_{\mathbf{q}}(t)\left\{\Phi_{\mathbf{q}}(t) + \int_0^t dt'\, m_{\mathbf{q}(\mathbf{t}')}(t-t')\,\dot\Phi_{\mathbf{q}}(t')\right\} = 0. \quad (1)$$

An initial Taylor dispersion is given by $\Gamma_{\mathbf{q}}(t) = D_0 q^2(t)/S_{q(t)}$. The generalized friction kernel $m_{\mathbf{q}'=\mathbf{q}(t')}(t)$ is an autocorrelation function of fluctuating stresses and depends on the shear-advected wavevector. Using approximations motivated by quiescent MCT leads to an expression which is a quadratic polynomial in the density correlators,

$$m_{\mathbf{q}'}(t) = \frac{1}{2N}\sum_{\mathbf{k}'} \frac{S_{q'(t)} S_{k'} S_{p'}}{q'^2(t)\, q'^2}\, V_{\mathbf{q}'\mathbf{k}'\mathbf{p}'}(t) V_{\mathbf{q}'\mathbf{k}'\mathbf{p}'}\, \Phi_{\mathbf{k}'}(t)\, \Phi_{\mathbf{p}'}(t), \quad (2)$$

with abbreviations $\mathbf{k}' = \mathbf{k}(t')$ and $\mathbf{p}' = \mathbf{p}(t') = \mathbf{q}(t') - \mathbf{k}(t')$. The vertex function is given by

$$\begin{aligned} V_{\mathbf{qkp}}(t) &= \mathbf{q}(t)\cdot\left(\mathbf{k}(t)\, n\, c_{k(t)} + \mathbf{p}(t)\, n\, c_{p(t)}\right), \\ V_{\mathbf{qkp}} &= V_{\mathbf{qkp}}(t=0), \end{aligned} \quad (3)$$

where c_k is the Ornstein-Zernicke direct correlation function, $c_k = (1 - 1/S_k)/n$, and n the particle density. The MCT-ITT equations are specified by the initial diffusion coefficient D_0 and the equilibrium structure factor, S_k, which introduces the experimental control parameters like density and temperature. Structural (and rheological) quantities are obtained in the ITT approach from following their evolution under flow starting from (known) initial equilibrium values. Because of the approach to a unique long-time state under steady shearing in ITT, general formal stationary expectation values can be derived. Performing related MCT approximations, explicit expressions, e.g., for the transient anisotropic distortion of the structure factor $\delta S_{\mathbf{q}}(t) \equiv S_{\boldsymbol{q}}(t) - S_q$ can thus be obtained following Ref. 24,

$$\delta S_{\boldsymbol{q}}(t,\dot\gamma) = \int_0^t dt' \frac{\partial S_{q(-t')}}{\partial t'} \Phi^2_{\boldsymbol{q}(-t')}(t'). \quad (4)$$

The structural distortion is found as time integral over the derivative of the equilibrium structure factor advected with the affine flow $S_{q(-t)}$, weighted by the square of the transient density correlator $\Phi_q^2(t)$ at each time instance t. The former factor thus depends on accumulated strain $\dot{\gamma}t$ only and decays on a strain scale which has been discussed by Refs. 2 and 25. The latter factor captures the memory stored in the system of the distortion of S_q at the earlier times before t. Its relaxation will depend on the structural relaxation time τ in the fluid phase for Pe $\ll 1$ or on the shear rate in the limit of Pe $\gg 1$. For long times, or large accumulated strains, the $\delta S_{\mathbf{q}}(t)$ thus assumes a well-defined stationary value denoted $\delta S_{\mathbf{q}}$ in the following. There is another contribution to $\delta S_{\mathbf{q}}(t)$ obtained by Ref. 24 which is isotropic and depends on q only. Such a term is expected and will, e.g., contribute to the shear-dependent pressure. The result by Ref. 24, however, fails to describe local distortions correctly and violates the condition that S_q should result from the incoherent scattering of individual particles in the limit of $q \to \infty$. Thus, the isotropic term will not be evaluated in the following even though the experiments clearly indicate its existence. Rather we will use projections onto spherical harmonics in order to isolate the anisotropic distortions of interest. Note that the error of the isotropic term in MCT-ITT also affects Ref. 26, where only the anisotropic term is reliable.

MCT-ITT provides a close connection of the structural distortions and the deviatoric stresses, which connects the local structural dynamics to the macroscopic mechanical response, via

$$\sigma_{ij}(t) = \frac{k_B T n}{2} \int \frac{d^3k}{(2\pi)^3} \frac{k_i k_j}{k} c_k' \, \delta S_{\mathbf{k}}(t, \dot{\gamma}), \tag{5}$$

where the direct correlation function c_k plays the role of an effective potential, and $k_B T$ is the thermal energy. This (approximate) relation between distorted structure factors and stresses in glass-forming systems differs from the rigorous relation derived in dilute dispersions in, e.g., Ref. 27, where stresses are calculated from shear-distorted pair correlation functions.

Numerical solutions of the microscopic MCT-ITT expressions for Brownian hard spheres have recently become possible by algorithmic developments described in detail by Ref. 25. They are based on the Percus-Yevick approximation for the equilibrium structure and lead to quantitative predictions of the steady-state rheology of colloidal hard spheres albeit with the approximation that hydrodynamic interactions are neglected. The results depend only on the packing fraction $\phi = \frac{\pi}{6}(N/V)d^3$, which is the single relevant thermodynamic parameter for hard sphere systems. Additionally, a short-time diffusion coefficient sets the time-scale. Stationary shear and normal stresses are described in Ref. 28, where also supplementary results on the transient stress evolution are contained. First, comparisons of the stresses with experimental rheological measurements have been described in Ref. 29. The present work complements this study with structural quantities and is the first to compare both structure and rheology simultaneously with mode coupling theory predictions.

B. Experimental system

We achieve simultaneous rheology and structure factor measurements by using an adapted commercial rheometer (Mars II, Thermo Fisher) placed in the beam path of a synchrotron (beam line P10 of the synchrotron PETRA III at DESY).[30,31] The well-collimated synchrotron beam with wavelength $\lambda = 0.154$ nm is deflected vertically to pass through the layer of suspension perpendicular to the rheometer plates (Fig. 1), allowing structure factor measurement in the shear-vorticity plane. The suspension consists of silica particles with a polydispersity of 10%, suspended in water. Two types of particles were used, with diameters of 50 and 92.5 nm.

A small amount (~2 mM) of *NaCl* is added to screen the particle charges, resulting in a Debye screening length of 2.7 nm, and effective particle diameters of $d_1 = 55.4$ nm and $d_2 = 97.9$ nm, respectively. Dense samples were prepared by dilution from centrifuged sediments assuming a particle volume fraction of 64% of the sediment. The relaxation time of the 50 nm sample was measured with x-ray scattering from the relaxation of the structure factor after applied shear, yielding $\tau \sim 10^6 t_B$,[30] indicating that the suspension is close to the colloidal glass transition.[32] Indeed, we estimate the effective volume fraction of this sample to be $\phi \sim 58\% \pm 2\%$, consistent with this measured relaxation time. The 92 nm particle sample was prepared with a higher volume fraction $\phi \sim 60\% \pm 2\%$. We estimate both volume fractions from the dilution of the sample centrifuged to a sediment and verify the estimated values by comparison of the normalized viscosity with other published data.[33] After loading, all samples are sealed with low-viscosity oil to prevent evaporation and maintain sample stability over more than 4 h. This allowed us to measure samples repeatedly and reproducibly. We initialized the samples by preshearing at a

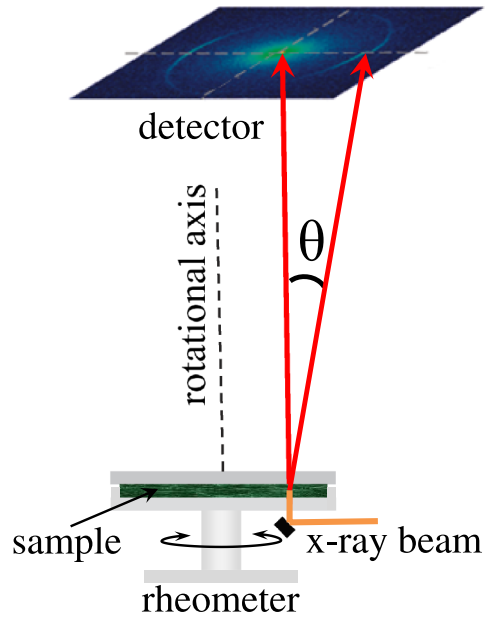

FIG. 1. Sketch of experimental setup where x-ray diffraction and rheology can be performed simultaneously on the glass-forming colloidal dispersions. The rheometer is stress controlled and we use plate-plate geometry with a plate separation of 0.5 mm. The disc radius is $R = 18$ mm, and the x-ray beam passes through the suspension at $0.78R$. The beam diameter is ~0.1 mm, much smaller than the disc radius.

rate of $\dot{\gamma} = 0.1\ s^{-1}$ for 120 s followed by a rest time of 600 s. We then applied shear at constant rates between $\dot{\gamma} = 3 \times 10^{-5}$ and $1\ s^{-1}$, corresponding to bare Peclet numbers between 10^{-6} and 10^{-2}; this range of Peclet numbers provided ideal comparison with MCT data. Yet, care should be taken during the transients. Because we used a stress-controlled rheometer, the steady-state shear rate was well controlled; during start-up, however, strain rates may deviate from the pre-set values. Namely, at the beginning of the experiment at low strains ($\gamma < 0.2$), the shear rate can be lower than its pre-set value. As a result, we find that the stress overshoot regime experimentally exists in a narrower range of strains ($0.45 < \gamma < 0.55$) than calculated in the MCT approach. Hence, only the steady-state data can be ideally compared with mode-coupling theory.

To follow the structure factor simultaneously with the applied shear, we use a Lambda detector at a distance of $L = 280$ cm and record the scattered intensity at a frame rate of 1 Hz. The detector with pixel size $172 \times 172\ \mu m^2$ covers scattering angles θ between 0.03° and 0.5°, corresponding to wavevectors $q = 4\pi/\lambda \sin(\theta/2)$ in the range $qd_1 = 1$ to 10. We determine the structure factor $S(\mathbf{q})$ from the recorded intensity by subtracting the solvent background and dividing by the particle form factor determined from dilute suspensions. The simultaneous measurement of both rheology *and* structure factor during the shear of the colloidal glass allows for a most stringent test of mode coupling theory predictions.

To compare experimental and theoretical results, all parameters need to be matched. The scale of length is set by the particle radius, and the energy scale is given by thermal energy k_BT. The volume fraction measures the importance of excluded volume particle interactions, and the Peclet number, the relative strength of flow compared to intrinsic diffusion. While the matching is straightforward for the thermal energy, it is less so for the particle radius and packing fraction in polydisperse dispersions, and it is even less clear for the Peclet number that contains the diffusion coefficient. Theoretically, the diffusion coefficient is $D_0 = k_BT/(3\pi\eta_s d)$, the Stokes-Einstein-Sutherland diffusion coefficient of a single sphere in a solvent with viscosity η_s. We hence define the Peclet number $\mathrm{Pe}_0 = \dot{\gamma} d^2/D_0$. In real experimental situations, hydrodynamic interactions between the particles slow down their free diffusion at short times, even before the particles collide.[34] It is often argued that at high particle concentrations, hydrodynamic interactions are accounted for by a renormalization of the short-time diffusion to an effective diffusion coefficient D^{eff}.[32] We adopt this strategy here for sheared suspensions. Assuming that this short-time diffusion coefficient is the relevant parameter, the effective Peclet number is then $\mathrm{Pe}_0^{\mathrm{eff}} = \dot{\gamma} d^2/D^{\mathrm{eff}}$. Following Ref. 32 for a similar system, we assume $D^{\mathrm{eff}} = D_0/10$, where D_0 follows from the particle size and viscosity of water, which we take as $\eta_s = 1$ mPa. In this manuscript, all experimental diffusion coefficients and Peclet numbers will be effective ones; to simplify the notation, we will drop the superscripts.

III. RESULTS

To test the matching of parameters, we first compare the macroscopic rheology. Once we have validated the correspondence of the rheological data (Section III A), we will turn to structural quantities underlying the plastic deformations (Section III B).

A. Macroscopic viscosity

Normalized values of experimental viscosities are obtained from the measured steady-state shear stress using $\eta = \sigma_{xy}/\mathrm{Pe}_0$ with the effective Peclet number Pe_0. For the theoretical values, shear viscosities are obtained by solving Eqs. (1)–(5), the latter by setting $k_ik_j = k_xk_y$ in the integral. Doing so, we compute shear-rate dependent viscosities for various densities around the glass transition, where $\varepsilon = (\phi - \phi_c)/\phi_c$ measures the relative separation to the MCT glass transition at ϕ_c. We show a comparison of the experimental viscosities with MCT predictions in Fig. 2. The window of Peclet numbers relevant to structural relaxation is given by $\mathrm{Pe}_0 \ll 1$, while the relaxation time τ shows up as crossover, below which a Newtonian viscosity plateau exists. We found that scaling the experimental viscosities by 0.4 brings the measurements at $\phi = 0.58$ onto the theoretical viscosity curve at the MCT glass transition. Black circles and triangles denote the measurements at 60% and 58% volume fraction, and colored symbols denote MCT predictions for various ε.

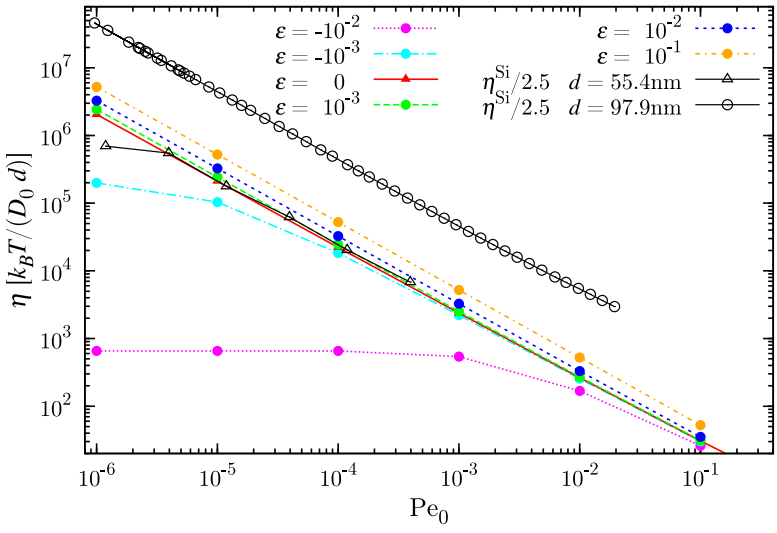

FIG. 2. Steady-state shear viscosity $\eta = \sigma_{xy}/\mathrm{Pe}_0$ vs bare Péclet number Pe_0 from experiment on silica particle dispersions and from MCT-ITT. The *black* data show experimental results for two different particle sizes, from Ref. 30 (*triangles*, $\phi = 0.58$) and *unpublished* (*circles*, $\phi = 0.60$), where shear rates were converted to $\mathrm{Pe}_0^{\mathrm{eff}}$ as described in the text. In order to compare η at $\phi = 0.58$, the experimental stress data are rescaled by a factor 0.4. Results (colored data) from theory are shown for six shear rates $\mathrm{Pe}_0 = 10^{\{-6;\ldots;-1\}}$ and for relative packing fractions ε as given in the legend. Symbols are connected with straight lines as guides to the eye.

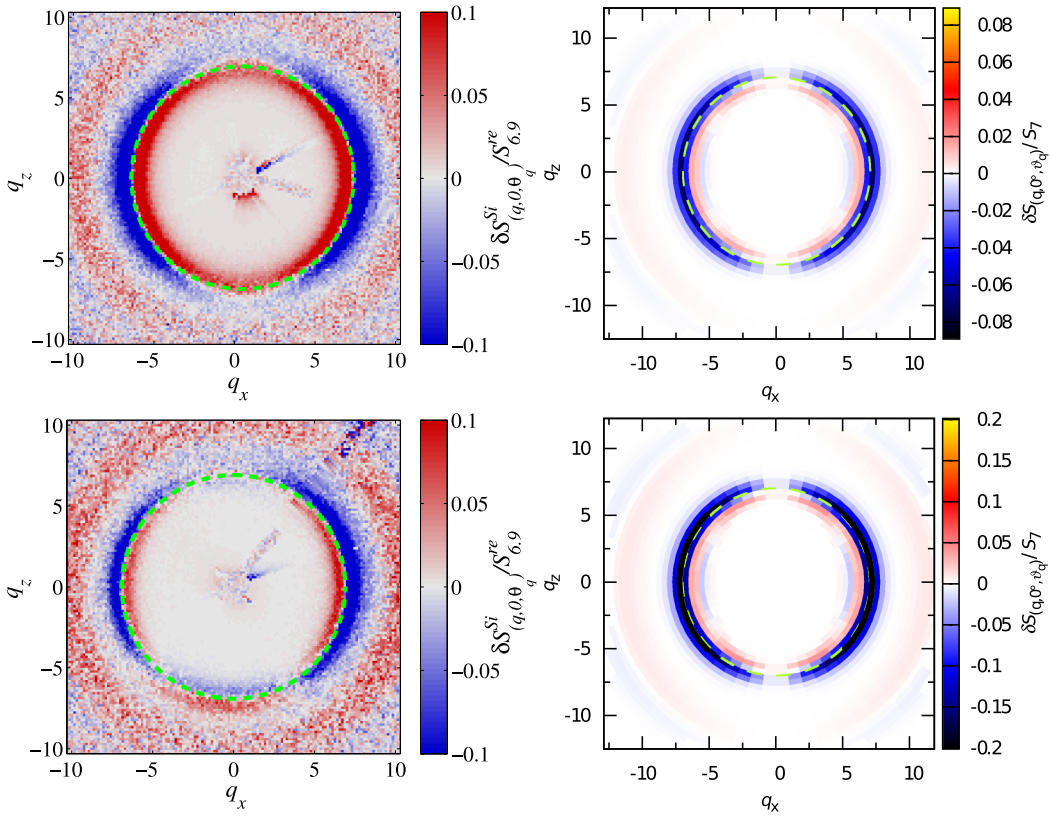

FIG. 3. The *left panels* show the stationary structure factor distortions $\delta S_{\boldsymbol{q}}^{\mathrm{Si}}$ of silica particle dispersions obtained by x-ray scattering in the q_x, q_z-plane, at packing fraction $\phi \simeq 0.58$. The upper left panel at shear rate $\dot{\gamma} = 3 \times 10^{-4}$/s which corresponds to the lowest Pe_0 data point for silica particles with $d = 55.4$ nm in Fig. 2. The lower left panel shows $\delta S_{\boldsymbol{q}}^{\mathrm{Si}}$ at shear rate $\dot{\gamma} = 10^{-1}$/s corresponding to the highest Pe_0 for this sample in Fig. 2. *Right panels* show corresponding theoretical $\delta S_{\boldsymbol{q}}$ in the q_x, q_z-plane for the steady state at $Pe_0 = 1.18 \times 10^{-6}$ (upper) and $Pe_0 = 3.96 \times 10^{-4}$ (lower panel) and at $\varepsilon = -6.7 \times 10^{-4}$, where the macroscopic viscosities of experiment and theory agree. The distortions are normalized to their quiescent structure factor peak values. The green dashed circles show the position q_{pk} of the quiescent S_q peaks. A distortion of $\delta S_{\boldsymbol{q}}$ along the q_x axis can be identified, which becomes stronger for higher $\dot{\gamma}$.

After rescaling, we observe good quantitative agreement for the 50 nm suspension with volume fraction $\phi \sim 58\%$, see the red curve at $\varepsilon = 0$ in Fig. 2. (Only the data point measured at the lowest shear rate somewhat lies below the curve, which will be discussed at the end of this paragraph.) This supports the finding by Refs. 28 and 29 using core-shell microgels that MCT-ITT predictions of steady-state viscosities are comparable to measurements in colloidal dispersions at the glass transition. The strong decrease of the viscosity over almost the entire range of Peclet numbers indicates that already very small shear rates interfere with the structural relaxation. For the 50 nm suspensions, we measure that the intrinsic relaxation time $\tau \sim 35$ s[30] is a factor of 2×10^6 larger than the Brownian time $t_B = 6.4 \times 10^{-5}$ s. Hence, the rescaled Peclet or Weissenberg number Pe lies around unity or above, indicating that indeed the applied shear starts to dominate the thermal relaxation. While these measurements appear to be close to the glass transition, the first data point (lowest shear rate), which drops below the theoretical curve for $\varepsilon = 0$, indicates that the experiments are performed slightly below the glass transition. This is still significant when we include the error bar, which for the lowest shear rate is rather high, around $\Delta\eta \sim \pm 3 \times 10^5 (k_B T / D_0 d)$. We estimate by linear interpolation that a theoretical curve at $\varepsilon = -6.7 \times 10^{-4}$ would be closest to the experimental data, with error margin $-1 \times 10^{-3} < \varepsilon < -1 \times 10^{-4}$ corresponding to the $\Delta\eta$-error estimate.

The higher volume fraction data (ca. 4% higher packing fraction) lie above the viscosities of the smaller particles, as expected. MCT-ITT recovers this trend of increasing viscosity with ϕ, yet the experimental trend is far stronger than expected by theory, as can be seen from the curves for $\varepsilon = 0.01$ and 0.1 (1% and 10% relative separation). This deviation is unclear at present but may be connected to the approach to random close packing, where particle contacts could increase the stress;[35] this is neglected by MCT-ITT.

B. Structure-factor distortion

1. Steady state

Steady-state viscosities thus show overall good agreement, albeit with a weaker predicted density dependence than seen in experiment. A stringent test of the theory is given by simultaneous comparison of the deformed structure. To compare structural changes resulting from the applied shear, we subtract the equilibrium structure factor, S_q, to compute $\delta S_{\mathbf{q}}(t) \equiv S_{\boldsymbol{q}}(t) - S_q$. Equilibrium structure factors of our silica suspensions have been reported in Ref. 30 and are well described by theoretical hard-sphere structure factors. For the MCT-ITT calculations, we used the widely available Percus-Yevick approximation even though it somewhat differs at the considered high packing fractions. By considering the

difference $\delta S_{\mathbf{q}}$ determined in experiment and in theory, errors due to the theoretical uncertainties in the description of the quiescent structure are minimized. The resulting excess structure factors $\delta S_{\mathbf{q}}$ over the equilibrium structure are compared in the wavevector plane spanned by q_x, the flow-velocity direction, and q_z, the vorticity or neutral direction in Figure 3, experiments (left) and MCT calculations (right). The shear rates displayed in the upper and lower row are, respectively, the lowest and the highest one, differing by more than two orders of magnitude. Experiments and theoretical predictions show a similar trend: At both shear rates and increasingly so with shear rate, the main peak of the structure factor moves inwards along the flow direction. This corresponds to a stretching of the neighbour shells in real space along $\hat{\mathbf{x}}$, the flow direction. This stretching appears rather reasonable, yet it results from a subtle competition of compression and dilation effects in the shear flow-shear gradient plane. Along the $\hat{\mathbf{x}}$ direction, the component q_y vanishes, meaning that we need to integrate all distortions in real-space along the flow-gradient (viz., y-) direction, which include elongation and compression of the particle packings, as described in detail in Sec. III B 3 below. Yet, distortions of the structure factor, while clearly measurable, remain rather small and are around ten percent of the equilibrium structure factor. This is in contrast to the viscosity, which is strongly affected by the shear rate.

We show a quantitative comparison of this structural anisotropy in Fig. 4, where we plot $\delta S_{\mathbf{q}}$ as a function of polar angle ϑ_q around the nearest neighbor peak position q_{pk} (green circles in Fig. 3). The structure factor is unchanged perpendicular to the flow direction and is reduced in all other directions. Theory predicts that the distortion is axis-symmetric to the flow direction and largest parallel ($\vartheta_q = 90°$) to it. Experimentally, we observe a slight tilt of the structure factor distortions, giving rise to an offset $\Delta\vartheta = 9.7°$ at the lower shear rate $\dot{\gamma} = 3 \times 10^{-4}$/s and $\Delta\vartheta = 39°$ at the higher shear rate $\dot{\gamma} = 1 \times 10^{-1}$/s. In Figs. 3 and 4, this tilt is eliminated in order to facilitate comparison with mode coupling predictions. We believe that the origin of this tilt is related to differences in the shear geometry, likely to the difference between the rotary shear geometry in the experiment and the simple translational shear geometry in MCT; we therefore omitted this tilt for clearer comparison of the structure factors.

After this adjustment, the agreement between theory and experiment is good for the lower shear rate (left panel). For the higher shear rate, theory predicts that the magnitude of the distortion grows by a factor of around 4. Contrarily, the experimental data show a smaller structural distortion at the higher shear rate. The origin of this difference may well be connected to the tilt of the scattering signal, which could indicate that theory and experiment consider different planes in reciprocal space. In the right panel of Fig. 4, the experimental $\delta S_{\boldsymbol{q}}$ are thus multiplied by a factor 5 in order to compare the shape to the theoretical one. The resulting experimental data show overall good qualitative agreement and deviate only slightly from the theoretically predicted symmetry around $\vartheta_q = \frac{\pi}{2}$ due to limited accuracy and noise. Another reason for the quantitative difference of the data can be the slightly soft particle potential in the experiment. Though the Debye screening length is short making the potential hard-sphere-like, the slightly soft potential can lead to deviations of the experimentally observed structure with respect to the predicted one at high strain rates. In line with this argument, we observe that the quantitative agreement improves for smaller shear rates, as confirmed by scattering data at intermediate shear rates 10^{-3}–10^{-2} (see the Appendix).

2. *Transient spherical harmonics in the q_x, q_z-plane*

The preceding results reveal the distinct structural symmetry underlying shear-induced distortions. To characterize this symmetry and follow it as a function of strain, we decompose $\delta S_{\boldsymbol{q}}$ into spherical harmonics. These spherical harmonic functions describe the full angular dependence of $\delta S_{\boldsymbol{q}}$, also outside the plane $q_y = 0$ resolved in the present experimental setup. The complete orthonormal set of spherical harmonics Y_{lm} uses two angles, ϑ, the angle to the neutral $\hat{\mathbf{z}}$-direction, and φ, the

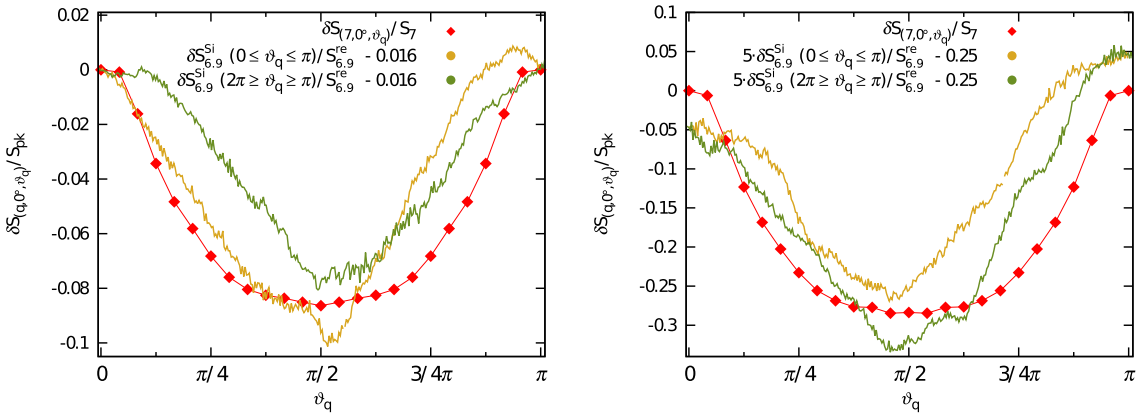

FIG. 4. Normalized structure factor distortion as function of angle ϑ_q in the q_x, q_z-plane; data from Fig. 3. The angle $\vartheta_q = 0$ corresponds to the $\hat{\mathbf{z}}$-direction perpendicular to the flow. Left panel: low $Pe_0 = 1.18 \times 10^{-6}$, right panel: high $Pe_0 = 3.96 \times 10^{-4}$. Experimental data are shown by lines (*golden* and *green* lines depict angular ranges of $\vartheta_q = 0 \ldots \pi$ and $\pi \ldots 2\pi$, respectively, for $q = 6.9/d$), while MCT calculations are shown by red diamonds and lines ($q = 7/d$). Wavevector magnitudes correspond to nearest neighbor distance (see green dashed circles in Fig. 3). All distortions are normalized to the equilibrium peak values S_{pk}. Experimental data are adjusted with an offset $\vartheta_q = 9.7°$ and isotropic background 0.016 in the upper panel, and with offset $\vartheta_q = 39°$ and isotropic background 0.25 in the lower panel; in the latter, the $\delta S_{\boldsymbol{q}}^{\mathrm{Si}}$s are additionally rescaled by a factor of 5.

angle to the flow direction, and can be written as[15,36]

$$Y_{l,m} \equiv \begin{cases} \mathcal{N}_{l,m} P_l^m [\cos(\vartheta)] \cos(m\varphi) & \text{for } m \geqslant 0 \\ \mathcal{N}_{l,|m|} P_l^{|m|} [\cos(\vartheta)] \sin(|m|\varphi) & \text{for } m < 0 \end{cases}, \quad (6)$$

with associated Legendre polynomials $P_l^{|m|}$ and normalization $\mathcal{N}_{l,|m|}$. For easy reference, the relevant ones with $l \leqslant 4$ read $P_0^0 = 1$ and

$$\begin{aligned} P_2^0 &\propto 3\cos^2\vartheta_q - 1, & P_4^0 &\propto 35\cos^4\vartheta_q - 30\cos^2\vartheta_q + 3, \\ P_2^2 &\propto \sin^2\vartheta_q, & P_4^2 &\propto \left(7\cos^2\vartheta_q - 1\right)\sin^2\vartheta_q, \\ & & P_4^4 &\propto \sin^4\vartheta_q, \end{aligned} \quad (7)$$

where the normalization can be shifted towards $\mathcal{N}_{l,|m|}$. By definition, the spherical harmonics are orthogonalized when integrated over the full solid angle.

The associated Legendre polynomials possess a parity of $(-1)^{l-m}$ under $\vartheta \to \pi - \vartheta$. MCT's transient density correlator $\Phi_{\boldsymbol{q}}(t)$ inherits an even parity under $\vartheta_q \to \pi - \vartheta_q$ or $\varphi_q \to \pi + \varphi_q$ from the equations of motion Eqs. (1)–(3). Consequently, $\Phi_{\boldsymbol{q}}(t)$ and thus the distorted structure from Eq. (4) can have only spherical harmonic contributions with even l and m.

Because scattering data are available in the q_x, q_z-plane only, multiple harmonics contribute to the observed plane, and an individual harmonic contribution cannot be projected out unambiguously. To compare the theoretical predictions to the experiments, we compute projections into the experimentally observed plane using

$$Y_{lm} \circ \delta S_{xz} = \int_0^\pi d\vartheta_q \sin\vartheta_q \, Y_{lm}(\vartheta_q, \varphi_q = 0) \delta S_{q_x q_z}. \quad (8)$$

This projection, in general, cannot eliminate an isotropic contribution ($l = 0$), which, reassuringly, was found to be small in Sec. III B 1.[37]

For glasses whose structure is typically distorted only mildly at small bare Peclet numbers, the dominant and interesting harmonics lie at small l. The linear (viscous) response $\delta S_{\boldsymbol{q}}$ of a colloidal fluid under shear is proportional to $Y_{2,-2}$ as has been discussed and simulated[15,26,36] repeatedly, as reviewed by Ref. 38. This spherical harmonic varies with $q_x \times q_y$ and thus vanishes in the experimentally observed plane; see below for more discussion of its time and wavevector dependence. The quadrupolar, real spherical harmonic Y_{22} is non-vanishing in the scattering plane and describes a distortion which is maximal in the flow direction and minimal perpendicular to it. It relates to the first normal-stress coefficient N_1, which indicates the difference in elongational stresses, $N_1 \equiv \sigma_{xx} - \sigma_{yy}$, and describes the effects of tensions in the material. The next contributions in the q_x, q_z-plane are hexadecupolar ones proportional to Y_{42} and Y_{44}. In the initial quiescent elastic response, the distortions seen in the q_x, q_z-plane start out quadratically in strain for small strains. They saturate to stationary values in the limit of large strains.

In the following, we focus on these quadrupolar ($l = 2$) and hexadecupolar ($l = 4$) contributions.[37] We take the density to be at the glass transition, $\varepsilon = 0$, and the shear rate to be far below the bare estimates, viz., $\mathrm{Pe}_0 \ll 1$, thus addressing glassy relaxation rather than small-scale diffusion affected at much higher Pe_0. Especially of interest is the evolution of the distortions with strain starting from the initial elastic to the final stationary state, where elastic and plastic contributions compete. Fig. 5 shows the corresponding stress versus strain curves following from Eqs. (1) to (5).[28] The shear stress σ_{xy} and first normal-stress coefficient N_1 (at $\varepsilon = 0^+$ and in the limit $\mathrm{Pe}_0 \to 0$) increase in the initial elastic regime quantified by the glass shear modulus G_∞, then exhibit a broad maximum, where part of the elastically stored stress is released, and finally approach the long-time limit of the stationary state. In the MCT-ITT calculation, the elastic regime lies below strain $\gamma \leq 0.1$ and the steady state holds for $\gamma \geq 1$, while in experiment, the corresponding γ values are smaller.[29]

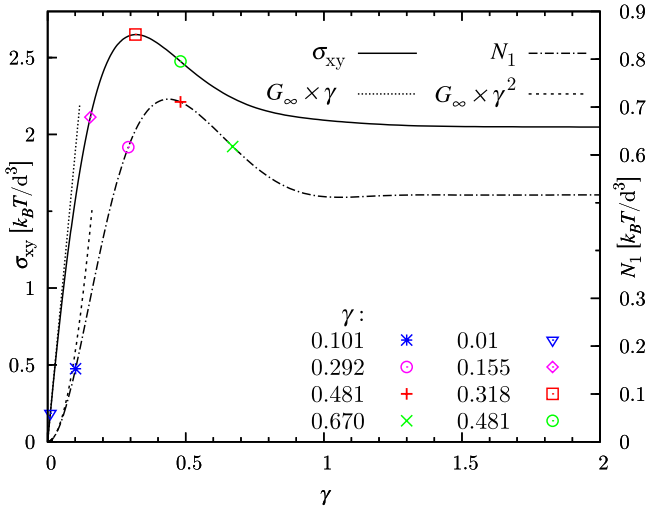

FIG. 5. Shear stress σ_{xy} (solid line and left axis) and first normal-stress coefficient N_1 (dotted-dashed line and right axis) versus accumulated strain $\gamma = \dot{\gamma} t$ in start-up flow with constant shear rate corresponding to $\mathrm{Pe}_0 = 10^{-6}$ and at the glass transition $\varepsilon = 0^+$ calculated by MCT-ITT. The behavior in the elastic regime is given by the elastic shear modulus G_∞ as indicated ($\sigma_{xy} = G_\infty \gamma$ and $N_1 = G_\infty \gamma^2$). Symbols mark the characteristic strains, for which the distorted transient structure is shown in Fig. 6 (symbols on N_1) or Fig. 8 (symbols on σ).

Projections on the leading harmonic contributions Y_{22} and Y_{42} of the q_x, q_z-plane are shown for several characteristic points on the stress-strain curve in Fig. 6. The strains represent the linear elastic regime ($\gamma \approx 0.1$), the overshoot regime ($\gamma \approx 0.3$, 0.5, and 0.7), and the final steady state ($\gamma > 1$). Left panels show the experimental data, and right panels the corresponding theoretical results. Experimental and theoretical curves exhibit similar q-dependence, i.e., a maximum followed by a minimum centered around q_{pk}, indicating a shift of the main peak to smaller q, and hence an elastic stretching of the neighbour shells in real space. Clearly, the distortions grow as the deformation proceeds from the linear to the nonlinear regime. The small distortion for small strains can be well rationalized by an initial quadratic variation of elastic nature. In contrast, the distortions of the final shear-melted glass differ strongly from the initial elastic response; we find this experimentally and theoretically. The differences obviously originate from the plastic rearrangements caused by the imposed shear deformation. Experimentally, the increasing scattering peak and its shift to smaller q indicate a better defined packing of the particles at a larger average distance. The theoretical results show a qualitatively similar, but more subtle variation: after the overshoot, the signal varies non-monotonously upon

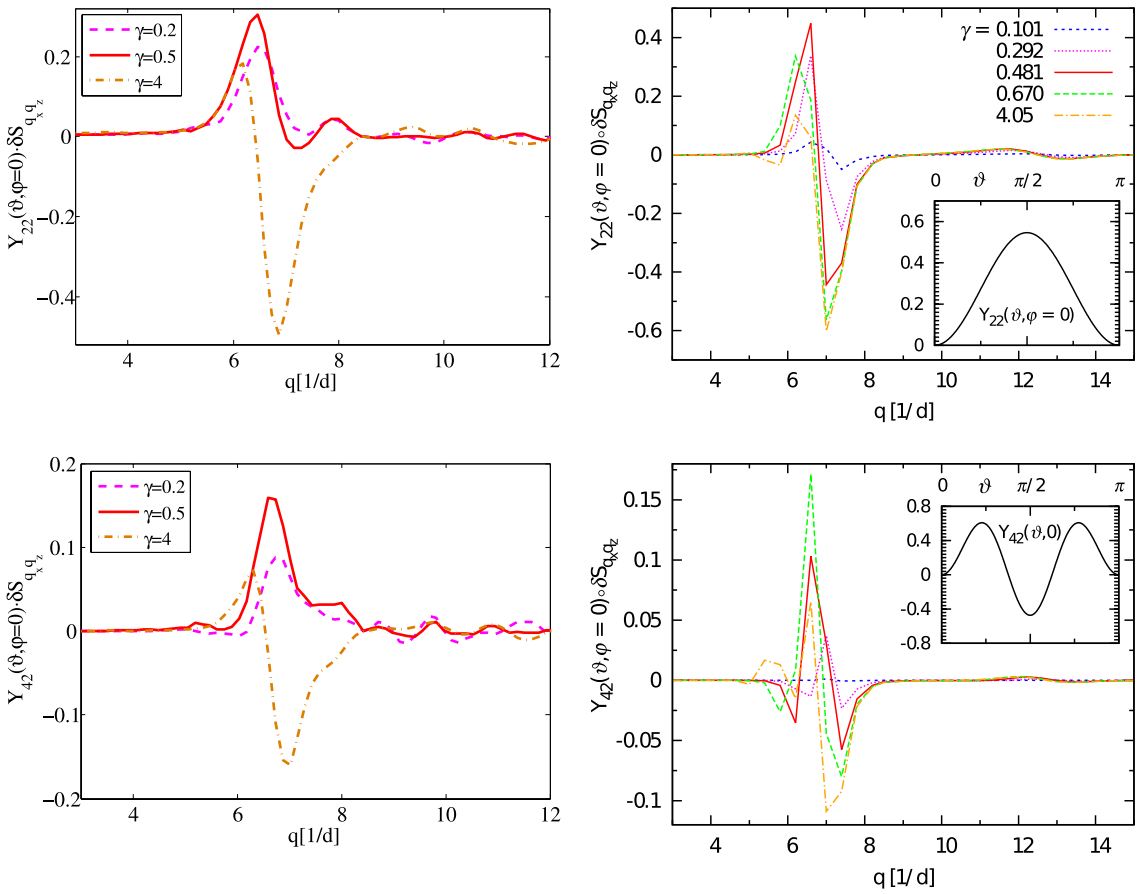

FIG. 6. Wavevector-dependent expansion coefficients of the transient distorted structure $\delta S_{\boldsymbol{q}}$ in the q_x, q_z-plane expanded in the spherical harmonics according to Eq. (8); the projection functions are shown in the insets. Curves for different strains show the evolution from the initial elastic to the final stationary state. The left panels show the experimental data for particles with $d = 55$ nm particles with 58% volume fraction at the shear rate 0.1 s^{-1} the strains are chosen starting from the linear ($\gamma = 0.2$) to the overshoot ($\gamma = 0.5$) to the stationary ($\gamma = 4$) regime. The right panels show corresponding MCT-ITT results at the transition ($\varepsilon = 0^+$) and in the limit of negligible shear rate, $\mathrm{Pe}_0 \to 0$; the strains are chosen starting from the linear ($\gamma = 0.1$) to the stationary ($\gamma = 4$) regime (the first normal-stress coefficient N_1 has a flat maximum at $\gamma'_* = 0.48$; see Fig. 5). The contour plots for the stationary two-dimensional data are shown in the lower row of Fig. 3.

approaching the stationary state, where theory and experiment are in semi-quantitative agreement. The transient differences presumably originate from the limited strain-rate accuracy of the stress-controlled rheometer. During the transient, strain rates can be somewhat lower than the pre-set steady-state value, hence deviating from the theoretical assumption of constant strain rate. This deviation leads also to a narrower stress overshoot in the stress-strain curves. The isotropic contribution not captured by theory also contributes to the expansion coefficients shown in Fig. 6. On the other hand, the almost quantitative agreement of the *steady-state* theoretical and measured structures in Fig. 6 may be somewhat fortuitous. As Fig. 4 showed, at the shear rate $\dot{\gamma} = 10^{-1}$/s, different amplitudes of the distortions are observed, presumably because of the different shear geometries. The present comparison is performed for different theoretical parameters ($\varepsilon = 0$ and $\mathrm{Pe}_0 = 0$ versus $\varepsilon = -6.7 \times 10^{-4}$ and $\mathrm{Pe}_0 = 3.96 \times 10^{-4}$) and thus gives an estimate of the uncertainty of the matching parameters. These uncertainties, however, do not affect the qualitative agreement of the functional forms.

The theoretically predicted non-monotonic trend of the distortion with Y_{22} symmetry is in line with an overshoot in the normal-stress coefficient N_1 that MCT-ITT finds around a strain of $\gamma'_* \approx 1.25\gamma_*$, where γ_* is the position of the stress overshoot (see Fig. 5). The increase of Y_{42} describes a density decrease in the vorticity direction; see the angular dependence of Y_{42} depicted in the lower inset in Fig. 6. This effect continues until after the overshoot in N_1, which could imply that the escape of the particles in the vorticity direction causes the reduction in the normal stresses. This interpretation would point to an effect comparable to, but weaker than, the particle motion discussed in Fig. 9. Interestingly, the Y_{42}-distortion in the stationary state mainly describes a shift in the next-neighbor peak position.

3. Transient spherical harmonics in the q_x, q_y-plane

The evolution of structural distortions reveals a characteristic change of the glass structure with the onset of plastic rearrangements.[2,29] The initial elastic stresses are partially released during the overshoot, as a result of the emerging structural rearrangements. Recalling that elasticity in colloidal glass results from the cage-effect hindering structural rearrangements in dense packings, the stress-overshoot signals the break-up of cages by the imposed shear. In this section, we take advantage of the full three-dimensional structure factor from MCT to show how the stress overshoot emerges as a consequence of the symmetry change of structural distortions. This enables

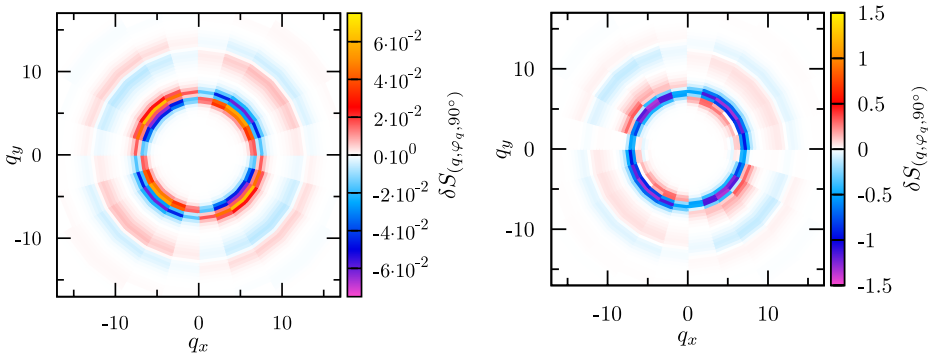

FIG. 7. Contour plots of the asymmetric SF distortion $\delta S_{\boldsymbol{q}} = S_{\boldsymbol{q}}(t,\dot\gamma) - S_q$ in the q_x, q_y-plane ($\vartheta_q = 90°$, shear-flow, -gradient plane) at the glass transition ($\varepsilon = 0$) and for a low shear rate ($\mathrm{Pe}_0 = 10^{-6}$). Different accumulated strains $\gamma = \dot\gamma t$ are shown: Left panel in the elastic region, $\gamma = 0.01$, right panel in the steady state, $\gamma = 3.44$.

us to identify cooperative non-affine particle motion behind the observed ensemble-averaged structural correlations, which may be considered to be *the plastic event that breaks the cage in shear-melted glass*.

Figure 7 compares the initial elastic distortions $\delta S_{\boldsymbol{q}}$ (left panel) with the final steady-state ones (right panel) in the q_x, q_y-plane. In the elastic regime, the expected quadrupolar structure, viz., $\delta S_{\boldsymbol{q}} \propto \sin\varphi_q \cos\varphi_q$, is clearly visible: four lobes appear with alternating sign at fixed q-radius. In contrast, in the steady-state regime, a hexadecupolar $l = 4$ symmetry appears, which has four equally signed lobes. Figure 8 below shows that this change of symmetry occurs around the peak strain γ_*, where the shear stress is maximal. The stationary distorted structure $\delta S_{\boldsymbol{q}}$ differs qualitatively from that of the elastic regime. This is true, in particular, at the main peak reflecting the nearest-neighbor structure. Our interpretation is that in the final steady-state regime, the elastic buildup of stress and its release in plastic events take place continuously and side by side. Thus, while the initial $\delta S_{\boldsymbol{q}}$ only contains elastic distortions, the stationary $\delta S_{\boldsymbol{q}}$ contains both, elastic and plastic, distortions. In addition, mode coupling theory also predicts an isotropic decrease of the structure, and higher-order distortions $l > 4$, but these appear negligible in the q_x, q_y-plane. Hence, the main change comes from the hexadecupolar contribution.

To investigate these changes quantitatively and in order to reveal the underlying particle rearrangements, we again use projections onto spherical harmonics, this time onto the flow-velocity and flow-gradient plane (q_x, q_y-plane), computed according to

$$Y_{lm} \circ \delta S_{xy} = \int_0^{2\pi} d\varphi_q \, Y_{lm}(\vartheta_q = \pi/2, \varphi_q) \delta S_{q_x q_y}. \qquad (9)$$

Because of the choice of the coordinate system, the $Y_{l,m}$ are orthogonalized under this planar projection.

Projections on the leading spherical harmonics are shown in Fig. 8. The curves reveal a characteristic strain evolution from the elastic to the plastic regime. The quadrupolar coefficient Y_{2-2} (left panel) is the leading contribution at small strain as expected; note its visible magnitude already at strains far smaller than considered in Sec. III B 2. The maxima followed by minima of this contribution indicate a shift of the structure factor to smaller q, revealing that the structure gets compressed along the diagonal ($q_x = q_y$) and stretched on the antidiagonal ($q_x = -q_y$). In real space, this means that the packing is stretched along the diagonal $x = y$, ("elongational direction"), while it is compressed along the antidiagonal $x = -y$ ("compressional direction"). This effect has been established in experiments and simulations[8,15,39] and is also found in MCT-ITT calculations in two dimensions.[26] With increasing strain, contributions from Y_{44} corresponding to $q_x^2 q_y^2 \propto \sin^2\varphi_q \cos^2\varphi_q$ symmetry emerge. They increase almost monotonically until they are the dominant contribution in steady state. Around γ_*, the hexadecupolar distortion becomes the largest one exceeding the elastic quadrupolar one. At the equilibrium peak position, the $_{44}$-symmetry contribution is the

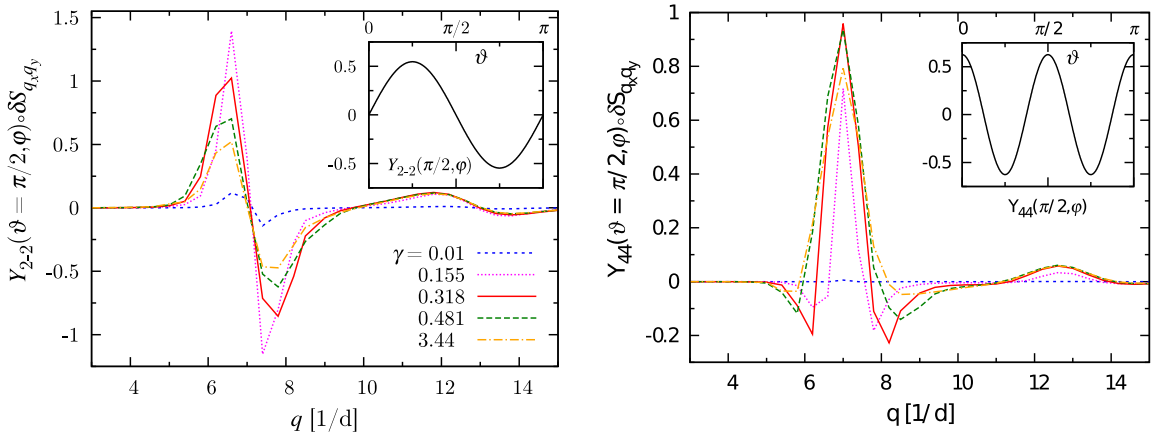

FIG. 8. Projection on spherical harmonics in the q_x, q_y-plane of the SF distortion $\delta S_{\boldsymbol{q}}$ of Fig. 7 for different strains as shown in the legend and marked by symbols in Fig. 5. A non-monotonicity in the Y_{2-2} projection can be identified which characterizes the stress overshoot. The hexadecapolar symmetry (Y_{44}) also decays, but much after the occurrence of the stress overshoot. The projection functions are shown in the insets.

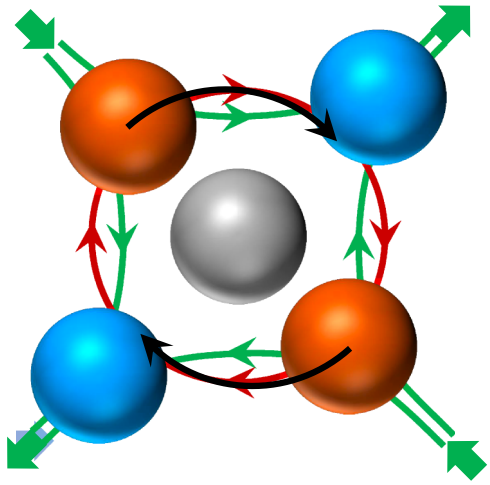

FIG. 9. Sketch of the cooperative particle motion that causes plastic relaxation under shear and enables particles to escape their neighbour cages. Shear flow is applied horizontally with gradient along the vertical. The particles come closer or move apart according to the compressional or elongational elastic deformation (indicated by green arrows showing only four particles indicating the dense neighbor shell). When the increase or decrease of the particle densities along the diagonals becomes too large, particle moves (indicated by black arrows) gain probability from the compressed to the dilated regions, which can follow the rotational component of the shear flow (red arrows). These particle rearrangements soften the elastic quadrupolar distortion and increase the structural intermediate-range order along all four diagonals (hexadecupolar symmetry).

largest, and the quadrupolar distortion vanishes. Within MCT, this is significant because it is the principal peak that captures the feedback on the cage effect in the theory. Also with respect to the rheology, the region around the nearest-neighbor peak plays a central role. It yields the largest contributions to the stress integrals in Eq. (5), because the transient correlators decay most slowly there.

We hence suggest the following particle-level interpretation: Considering that to first order, nearest-neighbor distances between particles adjust according to the elongational component (symmetric term in the velocity-gradient tensor), and remain unaffected by the rotational flow component (antisymmetric term of the velocity-gradient tensor), the distances between nearest neighbors decrease along the $x = -y$ axis and increase along $x = y$. This yields the quadrupolar symmetry in the structural distortion seen in the initial elastic regime (Fig. 7). Now assume that with increasing strain, this elliptic distortion becomes so large that the second-neighbor shell along the compressional direction overlaps with the depleted region of the first shell along the elongational direction. Then, there would be appreciable space opening up for the particles to follow the rotational shear-flow component and smoothen the density differences. This mechanism holds for all higher-order particle shells and their next-nearest shell and demarcates the transition from elastic to plastic flow. While this is the essential picture, the structure factors (Figs. 7 and 8) indicate that the rotational particle motion sets in earlier, even before the elastic distortion becomes as large. The onset of this cooperative process is reflected in the emergence of the hexadecupolar pattern that reinforces the neighbor shells along all four diagonals. Its intensity increases nonlinearly with strain and (almost) saturates around a characteristic strain γ_*, where the quadrupolar elastic deformation reaches a maximum. The fact that the hexadecupolar distortion has a maximum at the equilibrium nearest-neighbor peak indicates that the rotational motion takes place on all neighbor shells and does not affect their spacing. This hexadecupolar distortion remains active for all strains in the nonlinear regime beyond γ_*, especially in the steady state where the rotational particle motion causes the relaxation of part of the ongoing elastic deformation. This structural process is indicated by black arrows in Fig. 9; it might be called a *plastic event*.

IV. CONCLUSIONS

In this paper, we investigated the distorted structure of sheared glasses by combining x-ray scattering on colloidal glasses and mode coupling theory analysis in the integration through transients framework for shear-driven Brownian particles. We considered start-up flow with constant shear rate of the order of or larger than the inverse structural relaxation time of the glass, but much smaller than the inverse bare diffusion time at infinite dilution. In this regime, the samples remain amorphous and homogeneous, while the applied shear distorts the structure factor in all three directions: parallel to the flow-velocity, along the gradient direction, and perpendicular to the flow plane in the neutral (or vorticity) direction. In the steady state, the distorted pattern in the plane of flow-velocity and neutral direction indicates a stretching of the average particle separations along the flow. The intensity of the deformations in this plane is the largest parallel to the flow direction. Experiment on silica particle suspensions and theory on Brownian hard spheres record qualitatively similar trends. These structural distortions change symmetry from the initial elastic to the final stationary regime: In the flow-flow gradient plane, hexadecupolar symmetry appears and dominates over the initial (elastic) quadrupolar symmetry at yielding. We relate this to plastic rearrangements that are absent in the initial elastic regime, but compete with elastic deformations in stationary flow. These hexadecupolar contributions dominate at strain values where the start-up shear stress versus strain curves exhibits a maximum. We hence identify the structural signature of the yielding of glasses: The occurrence of a hexadecupolar pattern evidences the plastic rearrangements in the nonlinear regime.

ACKNOWLEDGMENTS

We thank the Deutsche Forschungsgemeinschaft (DFG) for partial financial support in the initiative FOR 1394, project P3. P.S. acknowledges support from FOM and the Netherlands Organization for Scientific Research (NWO).

APPENDIX: STEADY STATE STRUCTURE FACTOR DISTORTION AT INTERMEDIATE SHEAR RATE

We have also performed structural analysis at intermediate strain rates, which will be presented here. These intermediate data confirm the trend from low to high strain rates presented in the manuscript. Structural distortions at an intermediate

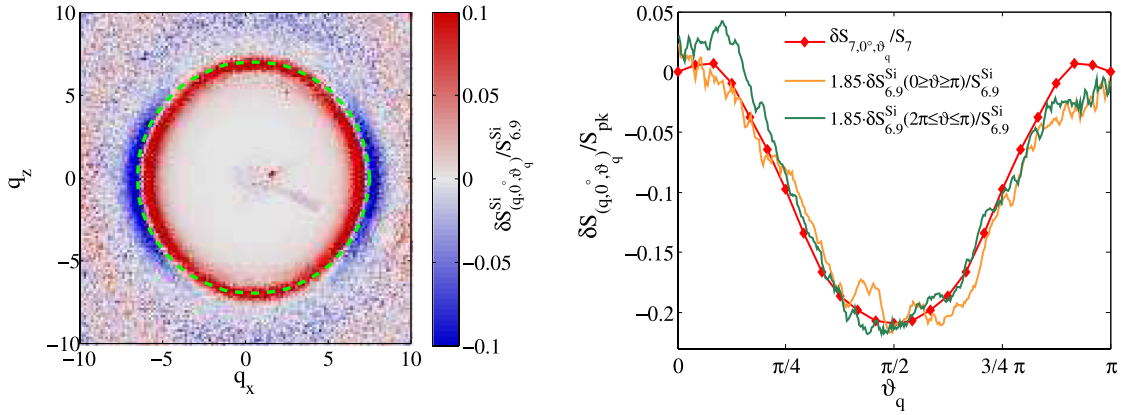

FIG. 10. Left: The scaled, stationary distorted structure factor $\delta S_{\mathbf{q}}^{\mathrm{Si}}$ of silica particle dispersions obtained by x-ray scattering in the q_x, q_z-plane is shown for $\dot{\gamma} = 3\times10^{-3}$/s (viz., $Pe_0 = 1.18\times10^{-5}$), $\phi \sim 0.58$. The dashed green circle shows the position of the quiescent structure factor peak. Right: Quantitative comparison of the structure factor distortion in the q_x, q_z-plane at the peak position of S_q from experiment (orange and green lines $q = 6.9/d$) to MCT calculation (red diamonds and line, $q = 7/d$); both as function of the angle ϑ_q to the $\hat{\mathbf{z}}$-direction. The distorted structure factors are shown normalized to their quiescent structure factor peak values. The MCT calculation is done at $\varepsilon = -10^{-3}$ and $\mathrm{Pe}_0 = 10^{-5}$. The colors of the experimental curves correspond to different ranges of ϑ_q (see legend). The experimental $\delta S_{\mathbf{q}}$ is multiplied with a scaling constant $c = 1.85$ to match the theoretical curve. The tilt is accounted for with an offset of $\vartheta_q = 23°$.

strain rate of $\dot{\gamma} = 3\times10^{-3}$/s are shown in Fig. 10. To map the experimental to the theoretical structure factor, we subtracted the tilt angle $\vartheta_q = 23°$ and scaled by a factor of $c = 1.85$. These values are indeed in between the values reported for the lowest and the highest strain rate reported in the manuscript, hence evidencing a systematic trend.

[1]J. Vermant and M. Solomon, J. Phys.: Condens. Matter **17**, R187 (2005).
[2]J. Zausch, J. Horbach, M. Laurati, S. U. Egelhaaf, J. M. Brader, T. Voigtmann, and M. Fuchs, J. Phys.: Condens. Matter **20**, 404210 (2008).
[3]G. L. Hunter and E. R. Weeks, Rep. Prog. Phys. **75**, 066501 (2012).
[4]P. Schall, D. A. Weitz, and F. Spaepen, Science **318**, 1895 (2007).
[5]R. Besseling, L. Isa, P. Ballesta, G. Petekidis, M. E. Cates, and W. C. K. Poon, Phys. Rev. Lett. **105**, 268301 (2010).
[6]X. Cheng, J. H. McCoy, J. N. Israelachvili, and I. Cohen, Science **333**, 1276 (2011).
[7]V. K. Chikkadi, G. Wegdam, D. Bonn, B. Nienhuis, and P. Schall, Phys. Rev. Lett. **107**, 198303 (2011).
[8]N. Koumakis, M. Laurati, S. U. Egelhaaf, J. F. Brady, and G. Petekidis, Phys. Rev. Lett. **108**, 098303 (2012).
[9]V. Chikkadi, D. M. Miedema, M. T. Dang, B. Nienhuis, and P. Schall, Phys. Rev. Lett. **113**, 208301 (2014).
[10]C. P. Amann, M. Ballauff, S. U. Egelhaaf, S. Fritschi, M. Fuchs, M. Krüger, P. Kuhn, M. Laurati, K. J. Mutch, K. Samwer, M. Siebenbürger, T. Voigtmann, and F. Weysser, "Hexadecupolar modes as signature of yielding in metallic and colloidal glasses," Phys. Rev. (submitted).
[11]R. Besseling, E. R. Weeks, A. B. Schofield, and W. C. K. Poon, Phys. Rev. Lett. **99**, 028301 (2007).
[12]M. Laurati, K. J. Mutch, N. Koumakis, J. Zausch, C. P. Amann, A. B. Schofield, G. Petekidis, J. F. Brady, J. Horbach, M. Fuchs, and S. U. Egelhaaf, J. Phys.: Condens. Matter **24**, 464104 (2012).
[13]F. Varnik, L. Bocquet, and J.-L. Barrat, J. Chem. Phys. **120**, 2788 (2004).
[14]F. Varnik and O. Henrich, Phys. Rev. B **73**, 174209 (2006).
[15]J. Zausch and J. Horbach, Europhys. Lett. **88**, 60001 (2009).
[16]O. Henrich, F. Weysser, M. E. Cates, and M. Fuchs, Philos. Trans. R. Soc., A **367**, 5033 (2009).
[17]W. Götze, *Complex Dynamics of Glass-Forming Liquids, A Mode-Coupling Theory* (Oxford University Press, 2009).
[18]P. N. Pusey and W. van Megen, Phys. Rev. Lett. **59**, 2083 (1987).
[19]W. van Megen and S. M. Underwood, Phys. Rev. E **49**, 4206 (1994).
[20]E. Bartsch, T. Eckert, C. Pies, and H. Sillescu, J. Non-Cryst. Solids **307**, 802 (2002).
[21]M. Fuchs, Adv. Polym. Sci. **236**, 55 (2010).
[22]M. Siebenbürger, M. Fuchs, and M. Ballauff, Soft Matter **8**, 4025 (2012).
[23]J. M. Brader, M. E. Cates, and M. Fuchs, Phys. Rev. E **86**, 021403 (2012).
[24]M. Fuchs and M. E. Cates, J. Rheol. **53**, 957 (2009).
[25]C. P. Amann, F. Weysser, M. Fuchs, M. Siebenbürger, M. Ballauff, and M. Krüger, J. Rheol. **57**, 149 (2013).
[26]O. Henrich, O. Pfeifroth, and M. Fuchs, J. Phys.: Condens. Matter **19**, 205132 (2007).
[27]J. F. Brady and J. F. Morris, J. Fluid Mech. **348**, 103 (1997).
[28]C. P. Amann and M. Fuchs, J. Rheol. **58**, 1191 (2014).
[29]C. P. Amann, M. Siebenbürger, M. Ballauff, and M. Fuchs, J. Phys.: Condens. Matter **27**, 194121 (2015).
[30]D. V. Denisov, M. T. Dang, B. Struth, G. H. Wegdam, and P. Schall, Sci. Rep. **3**, 1631 (2013).
[31]B. Struth, K. Hyun, E. Kats, T. Meins, M. Walther, M. Wilhelm, and G. Gruebel, Langmuir **27**, 2880 (2011).
[32]W. van Megen, T. C. Mortensen, S. R. Williams, and J. Müller, Phys. Rev. E **58**, 6073 (1998).
[33]G. Petekidis, A. Moussaid, and P. N. Pusey, Phys. Rev. E **66**, 051402 (2002).
[34]W. Russel, D. A. Saville, and W. R. Schowalter, *Colloidal Dispersions* (Cambridge University Press, 1989).
[35]A. Ikeda, L. Berthier, and P. Sollich, Phys. Rev. Lett. **109**, 018301 (2012).
[36]P. Strating, Phys. Rev. E **59**, 2175 (1999).
[37]The projection in Eq. (8) also cannot separate between Y_{22} and Y_{44} because of their similar ϑ-dependence. In MCT-ITT, where the full angular dependence is available and enables separation of the different spherical harmonics, one finds that the two corresponding expansion coefficients are very similar. Thus, their difference will be neglected in the following when projections in the q_x, q_z-plane are performed.
[38]G. Szamel, J. Chem. Phys. **114**, 8708 (2001).
[39]V. Chikkadi, S. Mandal, B. Nienhuis, D. Raabe, F. Varnik, and P. Schall, Europhys. Lett. **100**, 56001 (2012).